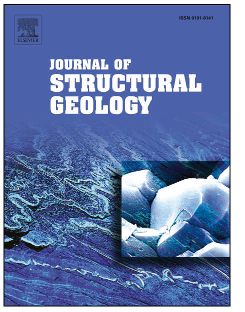

Mechanisms of strain accommodation in plastically-deformed zircon under simple shear deformation conditions during amphibolite-facies metamorphism

Elizaveta Kovaleva, Urs Klötzli, John Wheeler, Gerlinde Habler

PII: S0191-8141(17)30272-9

DOI: 10.1016/j.jsg.2017.11.015

Reference: SG 3562

To appear in: *Journal of Structural Geology*

Received Date: 17 March 2017

Revised Date: 21 November 2017

Accepted Date: 28 November 2017

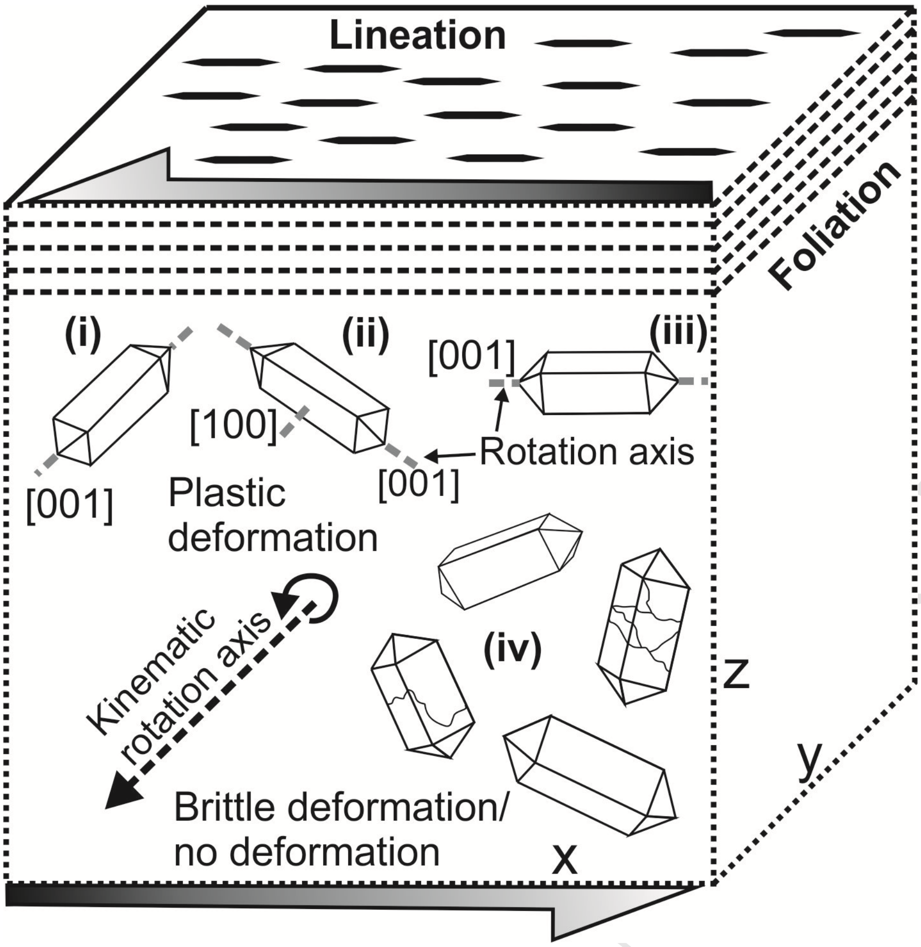

Lineation
Foliation
(i)
(ii)
(iii)
[001]
[100]
[001]
[001]
Rotation axis
Plastic deformation
Kinematic rotation axis
(iv)
z
y
Brittle deformation/ no deformation
x

Mechanisms of strain accommodation in plastically-deformed zircon under simple shear deformation conditions during amphibolite-facies metamorphism

Elizaveta Kovaleva*[1,2], Urs Klötzli[2], John Wheeler[3], Gerlinde Habler[2]

[1]Department of Geology, University of the Free State, 205 Nelson Mandela Drive, 9300 Bloemfontein, Free State, South Africa

[2]Department of Lithospheric Research, Faculty of Earth Sciences, Geography and Astronomy, University of Vienna, Althanstrasse 14, A-1090 Vienna, Austria

[3]Department of Earth, Ocean and Ecological Sciences, School of Environmental Sciences, University of Liverpool, L69 3GP, Liverpool, United Kingdom

* Corresponding author.

E-mail: kovalevae@ufs.ac.za; +27- (0)51 4019257

Abstract

This study documents the strain accommodation mechanisms in zircon under amphibolite-facies metamorphic conditions in simple shear. Microstructural data from undeformed, fractured and crystal-plastically deformed zircon crystals are described in the context of the host shear zone, and evaluated in the light of zircon elastic anisotropy. Our work challenges the existing model of zircon evolution and shows previously undescribed rheological characteristics for this important accessory mineral.

Crystal-plastically deformed zircon grains have <c> axis oriented parallel to the foliation plane, with the majority of deformed grains having <c> axis parallel to the lineation. Zircon accommodates strain by a network of stepped low-angle boundaries, formed by switching between tilt dislocations with the slip systems <100>{010} and <$\bar{1}$10>{110} and rotation axis [001], twist dislocations with the rotation axis [001], and tilt dislocations with the slip system <100>{001} and rotation axis [010]. The slip system <$\bar{1}$10>{110} is newly described for zircon. Most misorientation axes in plastically-deformed zircon grains are parallel to the XY plane of the sample and have [001] crystallographic direction. Such behaviour of strained zircon lattice is caused by elastic anisotropy that has a direct geometric control on the rheology, deformation mechanisms and dominant slip systems in zircon. Young's modulus and P wave velocity have highest values parallel to zircon [001] axis, indicating that zircon is elastically strong along this direction. Poisson ratio and Shear modulus demonstrate that zircon is also most resistant to shearing along [001]. Thus, [001] axis is the most common rotation axis in zircon.

Such zircon behaviour is important to take into account in structural and geochronological investigations of (poly)metamorphic terrains. Geometry of dislocations in zircon may help reconstructing the geometry of the host shear zone(s), large-scale stresses in the crust, and, possibly, the timing of deformation, if the isotopic systems of deformed zircon were reset.

Keywords

Zircon, elastic anisotropy, strain accommodation, slip, crystal-plastic deformation

1. Introduction

Zircon is a very common accessory minerals and it is widely used in geochronology (e.g. Davis et al., 2003). Consequently, the possible effects of the deformation of zircon are important to consider for isotopic analyses and mineral thermometry measurements, because it can dramatically affect the outcomes of these analyses. Crystal-plastic microstructures, such as dislocations and low-angle boundaries, can cause re-distribution of trace elements and their isotopes, including isotopes of U, Th, Pb, Ti and Y (e.g. Reddy et al., 2006, 2009; Moser et al., 2009, 2011; Timms and Reddy, 2009; Flowers et al., 2010; Reddy and Timms, 2010; Piazolo et al., 2012, 2016; MacDonald el al., 2013; Bellucci et al., 2016; Peterman et al., 2016; Kovaleva et al., 2017). For example, loss of Pb radiogenic isotopes and gain of Th and U can result in much younger isotopic age of deformed zircon than its formation age (e.g. Timms et al., 2006; Moser et al., 2009; MacDonald et al., 2013), and gain or loss of Ti through the dislocations can cause senseless results for Ti-in-zircon thermometry (e.g. Timms et al., 2011).

Crystal-plastically deformed zircon crystals are often observed in shear zones, and thus ductile deformation of zircon is attributed to the metamorphism and deformation of the host rock (e.g. Kaczmarek et al., 2011; Piazolo et al., 2012; Kovaleva et al., 2014, 2016). During these deformation event(s), zircon grains accumulate strain through elastic deformation, fracturing or formation of geometrically necessary dislocations (GNDs) and their subsequent migration (creep) into lower energy configurations (e.g. Hobbs, 1968; 1985; White, 1973; Poirier and Nicolas, 1975; Drury and Urai, 1990; Poirier, 1985). The geometry of GNDs in zircon can be determined with three methods:

(1) Transmitted electron microscopy (TEM) of focussed ion beam (FIB) foils (e.g. Leroux et al., 1999), which is the most precise, but also time-consuming and expensive method, requiring specific equipment.

(2) In an absence of TEM, GNDs can be assumed from the electron backscatter diffraction (EBSD) maps using Weighted Burgers Vector (WBV) calculations (e.g. Wheeler et al., 2009; 2012; MacDonald et al., 2013), which is especially useful when no low-angle boundaries are present. Such method, however, does not determine dislocations, which Burger's vector is parallel to the mapped surface. This method requires a special software (see Methodology section).

(3) Where well-developed low-angle boundaries are present, GND's geometry can be inferred from boundary geometry relative to the crystallographic geometry of the host grain ("boundary trace orientation analyses", e.g. Reddy et al., 2007).This method is the simplest of all three, fairly reliable and requires obtaining EBSD maps only.

In our contribution we make use of methods (2) and (3).

The resulting geometry of GNDs and their slip systems in zircon would be determined by (a) elastic anisotropy of zircon (e.g. Reddy et al., 2007) and (b) crystallographic orientation of the zircon in the shear zone (e.g. Kaczmarek et al., 2011; Kovaleva et al., 2016).

Elastic anisotropy properties of zircon under low temperature (≤ 300 °C) are generally well-constrained (e.g. Özkan and Jamieson, 1978; Bass et al., 1995; den Toonder et al., 1999). However, analysis of zircon deformation as a function of its elastic anisotropy at greater temperatures is not as well developed (e.g. Reddy et al., 2007; Timms et al., 2012). Consequently, the temperature dependence of elastic properties for zircon is also unknown.

Among rock-forming minerals, olivine, quartz, plagioclase and calcite deformation properties are the most studied in regard to their crystallographic orientation and elastic anisotropy (e.g. White, 1973; Hansen and Warren, 2015; Kruse et al., 2001; Bestmann and Prior, 2003; Menegon et al., 2011; Prior et al., 2011 and references therein). The more limited studies of zircon deformation evolution in shear zones include Kaczmarek et al. (2011), which was recently updated by Kovaleva et al. (2016). These studies evaluated the orientation of misorientation axes in crystal-plastically deformed zircon with respect to a sample vorticity axes. In particular, Kovaleva et al. (2016) demonstrated that crystal-plastically deformed zircon grains have <c> axes roughly parallel to the foliation plane of the sample, whereas undeformed grains have their <c> axes at a high angle to the foliation plane. The modelling (Kaczmarek et al., 2011) and empirical observations (Kovaleva et al., 2016) did not describe geometries of dislocations and other microstructures with regard to zircon elastic anisotropy, nor did they discuss specific mechanisms of strain accommodation in zircon at certain conditions. To our knowledge, there are no studies that correlate grain orientation in a shear zone, dislocation orientations in deformed zircon crystals and zircon anisotropy properties.

The present study focuses on one sample from the dataset presented in Kovaleva et al. (2016), and describes in detail microstructures in one population of zircon grains from a highly-strained meta-lamprophyric dyke (Kovaleva et al., 2014, 2016). Within the studied population, we made EBSD maps of 16 grains, 13 of which are crystal-plastically deformed, and additional orientation contrast images of 15 grains. In total, 31 zircon grains were microstructurally analysed. These analyses let us characterize crystal-plastic deformation of zircon under amphibolite-facies conditions. We use these outcomes to further describe zircon deformation behaviour, identify a new slip system, and relate intragranular deformation to the elastic anisotropy of zircon in the context of a shear zone deforming in these metamorphic conditions.

2. Geological setting of the sampling locality

The sample of this study is from a strike-slip shear zone in the “Zillertaler Kern” of the Western Tauern Window, Eastern Alps (Zillertal, Tyrol, Austria). The Eastern and Western Tauern Windows expose the footwall of the Austroalpine nappe system, composed here of continental and oceanic rocks of Penninic and sub-Penninic nappe sequences. Nappe stacking and regional metamorphism are related to the closure of the Alpine Neotethys and subsequent continental collision during early Tertiary (Miller et al., 2007; Veselá et al., 2011).

The detail description of the sampling locality, documented shear zone and analysed sample are presented in Kovaleva et al. (2016), their Figures 1 and 4A-B. Most importantly, the shear zone experienced sinistral simple shear during an Alpine tectono-metamorphic event under amphibolite-facies conditions of 0.5–0.7 GPa and 550–600 °C, and the thermal peak occurred at ca. 30 Ma (Selverstone et al., 1991; Pennacchioni and Mancktelow, 2007). Subsequently, the zone experienced retrograde metamorphism under greenschist-facies conditions during rapid exhumation of the unit at ~ 20 Ma (e.g. Selverstone, 1988, 1991; Pennacchioni and Mancktelow, 2007).

3. Methodology and data representation

3.1. Sample preparation

Two thin section slabs were cut normal to the XY plane and at 45° to the XZ plane. Such cut orientations were used to enable characterization of all elements of the microstructural population in these plastically-deformed zircon crystals (Supplemental Fig. 1). For example, thin section slabs cut parallel to the lineation (classic thin section cut), are less useful because they will not reveal microstructures and subgrain walls that are normal to the vorticity axis of the sample (e.g. Kaczmarek et al., 2011). The thin sections were mechanically polished with 0.25 µm diamond paste and chemically polished on a rotating disc with the colloidal silica solution Köstrosol 3530.

3.2. Scanning electron microscopy

Backscattered electron (BSE) images were collected with the FEI Inspect S scanning electron microscope (SEM). Electron backscatter diffraction (EBSD) maps and orientation contrast images of zircon grains were acquired with a FEI Quanta 3D field emission gun (FEG) SEM. Both instruments are located at the Faculty of Earth Sciences, Geography and Astronomy, University of Vienna, Austria. Details of analytical settings are presented in Kovaleva et al. (2014, 2016).

3.3. EBSD and elastic anisotropy data representation

The EBSD data are presented as: (1) EBSD pattern quality maps, showing the quality of the collected Kikuchi diffraction patterns, (2) colour-coded cumulative misorientation maps, showing relative misorientation of each pixel to a user-selected reference point within the crystal, or (3) local misorientation EBSD maps, where each pixel is color-coded according to the mean misorientation of each data pixel relative to its six neighbouring pixels. During processing and plotting of the data, no noise reduction or smoothing was applied due to the very high quality of the dataset (99.99% of pixel indexing). The pole figures with orientation of crystallographic axes are plotted in the lower hemisphere equal-area projections. Cumulative EBSD maps, EBSD pattern quality images and pole figures were produced with the EDAX OIM v6.2.1 Analysis software. The foliation plane in all pole figures is oriented horizontally. The local misorientation EBSD map and the visualization of density contours of misorientation axes orientation in the inverse pole figures were produced using the MATLAB MTEX toolbox (Bachmann et al., 2010, 2011; Mainprice et al., 2011). Elastic properties of zircon are visualised with MATLAB MTEX toolbox using the elastic constraints of Özkan and Jamieson (1978), Bass et al. (1995) and den Toonder et al. (1999).

3.4. Weighted Burgers Vector (WBV) calculations

We gained insight into geometrically necessary dislocation densities using WBV calculations (Wheeler et al., 2009; 2012). WBV quantifies the total Burgers vector for all the dislocations passing through the user-selected rectangular region in the EBSD map (the "integral form", according to Wheeler et al., 2009). This value can be expressed in terms of lattice vectors and then divided by the sample region area to measure dislocation density including Burgers vector direction. The components of summary WBV across the user-selected rectangular areas are expressed by three numbers: *a*, *b* and *c*, which are listed for each selected subarea and are measured in $(\mu m)^{-2}$. Rectangular areas with WBV components were calculated using EBSD maps with the MATLAB toolbox CrystalScape 1.3 based on the method described in Wheeler et al. (2009, 2012). For this calculation, the maps were transformed to a rectangular grid and the Euler angles were recalculated with the Channel software. For better visual representation, the rectangular areas were superimposed on top of a hexagonal "local misorientation" EBSD map.

The WBV can be calculated for any crystal system, but the method has several limitations. WBV is calculated from orientation gradients in a map view, i.e. it only documents dislocations that intersect a 2D surface of the map. Therefore, all dislocations that are parallel to the map are not analysed by the software, and no assumptions are made about gradients in the third dimension, which may be non-zero (see Wheeler et al., 2009, 2012). However, our sampling geometry let us document dislocations that lie in the XZ plane (see section 3.1).

Calculation of the WBV involves no assumptions about minimization of dislocation energy. The only assumption involved in the calculation is that elastic strains are small, so that the lattice distortion is entirely due to dislocations (Wheeler et al., 2012). Therefore, we assume that a non-homogeneous distribution of WBV values in analysed zircon grains are caused by stress-related dislocations.

4. Elastic anisotropy of zircon and its implications

The elastic anisotropy of zircon can be visualized by constraining Young's modulus and P-wave velocity contours (Fig. 1A-B). Large values for Young's modulus and P-wave velocity parameters are parallel to zircon {100} planes with the greatest values in the basal plane {001} and along the crystallographic directions <100> and [001]. High P-wave velocity values along the main crystallographic planes (Fig. 1B) indicate that these planes are the most densely occupied by atoms. At the same time, high Young's modulus correspond to crystallographic directions where the lattice is elastically stronger. Preferred slip in crystal lattices is expected to occur parallel to the crystallographic direction with the most closely spaced atoms, so that the Burgers vector has the shortest possible length (e.g. Poirier, 1985). In zircon, these directions are [100] and [001] (Fig. 1). Consistently, <100> was experimentally shown to be the energetically-preferable orientation of the Burgers vector, as the shortest translation vector in the zircon structure (Leroux et al., 1999). Therefore, slip or fracturing will more likely occur in zircon along these low indices planes. Thus, elastic anisotropy of zircon suggests preferable activation of slip systems <100>{010}, <010>{001} and <001>{010}. The densest plane is the basal plane {001}, and, consistently, deformed grains most often have a rotation axis parallel to [001] (e.g. Reddy et al., 2007; Kaczmarek et al., 2011; Kovaleva et al., 2016).

These properties are confirmed by the shape of Poisson ratio and Shear modulus contours (Fig. 1C-D). Poisson ratio, being greatest parallel to [001] and the smallest parallel to [100] (Fig. 1C), indicates that the strain along [001] always exceeds strain along [100]. This property defines the energetically-preferable rotation axis in zircon, which is [001]. Shear modulus is maximum parallel to [001], showing that zircon is most resistant to shearing along this axis, and thus confirming that this axis is the most preferable for a rotation axis.

This elastic anisotropy for Young’s modulus and Shear modulus of zircon was demonstrated before by Timms et al. (2012). However, the Young’s modulus anisotropy shape presented in Timms et al. (2012) reflect properties of metamict zircon. Their image, therefore, does not characterize the non-metamict zircon populations, such as the population presented in this study. Our population is characterized by a high crystallinity degree, reflected by Raman spectroscopy analyses (Kovaleva et al., 2014) and by high EBSD pattern quality images of all analysed grains (see microstructural data).

5. Sample description

The studied sample is a metamorphosed, strained and isoclinally-folded lamprophyre (see Kovaleva et al., 2016). Sample is composed of amphibolite-facies mineral assemblage, including plagioclase, biotite, titanite and quartz (Fig. 2A-B). Biotite and titanite form layers 1–6 mm thick, which alternate with mylonitized plagioclase–quartz layers with similar thickness (Figs.

2A-B, Supplemental Fig. 1). Biotite is chloritized as a result of retrograde greenschist-facies metamorphism, which occurred during exhumation of the unit (Fig. 2C). The accessory minerals are apatite, zircon, calcite, pyrite, and rutile (Fig. 2C-D). The foliation plane of the sample is formed by biotite-rich layers and is used here as the kinematic reference plane (Bestmann and Prior, 2003).

Zircon in the sample is present as small (10–30 μm) mostly euhedral grains, slightly elongate to the aspect ratio of up to 1:3 (Figs. 2C-D, 3-6). Zircon grains are enclosed in chloritized biotite (Fig. 2C-D), plagioclase, titanite or quartz (Table 1). The observed zircon population was initially magmatic in origin, but in some crystals, we observe metamorphic rims that grew on magmatic oscillatory-zoned cores (for CL images see Supplemental Fig. 2), and formed coevally with the host biotite grains, presumably, during peak amphibolite-facies metamorphism. Some zircon grains were subsequently fractured (Fig. 4) or crystal-plastically deformed (Figs. 5-6). Crystal-plastic deformation in zircon presumably occurred during amphibolite-facies Alpine metamorphism (30 Ma), however, the overprint of the greenschist-facies deformation (30-20 Ma) might have also taken place and influenced zircon deformation patterns. This overprint is a potential complication in our study. However, zircon deformation patterns are similar for amphibolite and upper-greenschist-facies conditions and are difficult to distinguish. Moreover, in our case, the transition between two regimes was gradual, thus, we assume that the potential greenschist-facies metamorphic overprint, if it happened, did not change the overall mode of zircon deformation. The population of zircons displays little radiation damage and is characterized by a high crystallinity degree, documented by high-quality EBSD patterns (Figs. 3; 5; 6C).

6. Microstructural and crystallographic zircon data

For this study, we have microstructurally investigated total of 31 zircon crystals (see Table 1). Zircon grains were decoupled from the host matrix (Kovaleva et al., 2014). Absence of coating, dragging of the surrounding biotite, open interface voids and pressure shadows provide evidence of zircon-matrix decoupling (e.g. Figs. 3A-B; 4A; 6C), which enables inhomogeneous stress distribution within zircon grains, especially when hosted by the rheologically softer material (e.g. see numerical modelling by Schmid and Podladchikov, 2005) and may lead to their crystal-plastic deformation (Kenkmann, 2000). The decoupling also indicates that post-deformational rigid-body rotation was absent, preserving the syn-deformation orientation of the zircon grains in the shear zone (see Kovaleva et al., 2016). Zircon grains from the sampled meta-lamprophyre are unstrained (e.g. Fig. 3), fractured (e.g. Fig. 4), or crystal-plastically deformed (e.g. Figs. 5-6), where about 45% of the zircon grains are crystal-plastically deformed (Table 1). The studied zircon population does not display crystallographic preferred orientation (e.g. Fig. 7A, Table 1).

Undeformed (e.g. Fig. 3) and fractured (e.g. Fig. 4) zircon crystals have <c> axes that are oriented at a high angle (≥ 15°) to the foliation plane XY, otherwise stretching in all other directions (e.g. Fig. 7A, open circles; Table 1). Within the fractured grains, fractures are generally subparallel to {100} crystallographic planes (e.g. Fig. 4A-B). Long axis <c> of all plastically-deformed crystals are parallel or subparallel to the foliation plane (e.g. Figs. 5; 6B; 7A, solid circles; Table 1). Moreover, orientations of <c> axis of ~ 55% of analysed crystal-plastically deformed grains are parallel or subparallel to the stretching lineation with their <c> (Figs. 5A; 6B, grains 03 and 04; Table 1). The rest of the plastically-deformed grains are oriented with <c> axis either at ~ 45-55° to the lineation (e.g. Fig. 5B, grain 15; Table 1), or at ~ 90° to the lineation (e.g. Fig. 5C, grain 24; Table 1).

The finite deformation pattern in plastically-deformed zircon grains is characterized by the presence of the strain-free subgrains that do not share lattice geometry orientations (e.g. Fig. 6A). This type of zircon deformation corresponds to distortion pattern type III (Piazolo et al., 2012). Low-angle boundary traces, which separate subgrains in the sampled zircon grains, reveal a continuous network of stepped lines, and, as a result, subgrains form irregular-shaped domains from 1 to 10 µm in diameter (Figs. 5; 6A). In rare cases, the low-angle boundaries are rounded or curved, forming oval-shaped subgrains (e.g. Table 1).

Misorientation axes of plastically-deformed grains are mostly parallel to the XY (foliation) plane, and sometimes are parallel to the YZ plane (Fig. 7B) for grains with comparatively low degree of strain (Table 1). In cases, where misorientation axes are parallel or subparallel to Y direction, they lie simultaneously in XY and YZ planes. Most intensely-strained grains have misorientation axes distributed around X, the direction of stretching lineation.

Most crystal-plastically deformed zircon grains (~77%) have misorientation axes clustering around the [001] crystallographic direction (Figs. 5; 6D; Table 1). Other misorietnation axes directions are <212>, <311> or close to these (such as <310>, <201> and <321>, see Table 1), but these directions are usually less significant and form minor clusters. For example, the misorientation axes of grain 24 are dispersed in the inversed pole figure, forming one strong cluster parallel to [001] and a few smaller maxima about <212> <321> and <110>. In grain 15, the misorientation axes cluster around [001] and [100] (Fig. 5B). Consistently, crystallographic axes in the pole figures for grains 15 and 24 are dispersed around multiple axes (Fig. 5A, C), which points to strain acting in localized parts of the grain with different slip systems, so-called “asterism” of crystallographic axes (e.g. Moser et al., 2009). In contrast, grains 03 and 04 reveal rotation of the crystallographic axes around the [001] direction in the pole figures and only one cluster of misorientation axes (Figs. 5A; 6B, arrows). This suggests that plastically-deformed grains with the orientation of <c> close to the stretching lineation, develop only one misorientation axis, which is usually parallel to [001]. The larger is the angle between <c> axis and the lineation, the more clusters of misorientation axes are observed (see Table 1).

If the main host phase for zircon is biotite, or chlorite as a result of biotite alteration, then a high probability of activation of misorientation axis [001] is observed (Table 1). Therefore, there also seem to be a strong control of the host phase’s rheology on zircon deformation (e.g. Kenkmann et al. 2000; Kovaleva et al., 2014; 2016). Rheologically softer host phases allow for the activation of the preferable rotation axis.

6.1. Analyses of the slip systems geometry

Geometrically necessary dislocations (GNDs) form in the crystal lattice to accommodate lattice strain. During strain recovery, GNDs may be clustered by dislocation creep, forming dislocation walls or low-angle boundaries. Therefore, the presence of low-angle boundaries in plastically-deformed grains provides an opportunity to identify dislocation slip system(s) that contributed to boundary formation. The geometry of low-angle boundaries reflects the slip-system geometry that can be reconstructed (e.g. Reddy et al., 2007; Kaczmarek et al., 2011; Timms et al., 2012). However, we should emphasize that the two-dimensional boundary traces may not always unequivocally identify the slip system(s) related to boundary formation.

In this contribution, we focus on detailed analyses of four crystal-plastically deformed grains, representative for our sample, as they reveal the most typical microstructures for this population. The amount of strain within these grains is comparatively high for the population. Therefore, it is easier to provide reliable geometry analyses of low-angle boundaries and GNDs. Additionally, we present microstructural orientation data on nine more crystal-plastically deformed grains from this sample (Fig. 7; Table 1), which show similar behavior. We provide boundary orientation trace analyses for grains 15, 24 (Fig. 5B-C) and 04 (Fig. 6B) and WBV analyses for grain 04 (Fig. 6A), in order to demonstrate that these two methods are in good agreement with each other.

Grain 03 is highly strained, compared to the other zircon grains in the population, and has a dense network of low-angle boundaries (Fig. 5A, left panel, pointed by arrows) with an average of four to five along any normal sampling line of about five microns length. The traces of low-angle boundaries form irregular, stepped lines with a complicated geometry. Obviously, several interchanging slip systems operated in this grain, switching along low-angle boundaries where they change their direction. All of these slip systems have rotation axes around [001], as indicated by the systematic rotation of the all crystallographic axes about zircon [001] (Fig. 5A, pole figure in the middle panel, arrows). Moreover, an inversed pole figure for this grain shows clustering of the misoritention axes close to [001] (Fig. 5A, right panel). As we have discussed earlier, [001] is the most commonly documented rotation direction (e.g. Leroux et al., 1999; Reddy et al., 2007; Kovaleva et al., 2016) and energetically-preferable rotation axis in zircon, due to elastic and crystallographic anisotropy of non-metamict zircon (Fig. 1; Reddy et al., 2007). Usually, subgrain wall, consistent with one dislocation geometry would also have a consistent direction. In this grain, subgrain boundaries reveal complicated geometry: stepped configurations and change of direction over small distances. Therefore, we suggest that subgrain boundaries in grain 03 (Fig. 5A) represent both tilt and twist ("mixed") walls (e.g. see boundary trace analyses in Reddy et al., 2007).

In grain 15, low-angle boundary traces extend in two general directions (NNW-SSE and WSW-ENE in the Fig. 5B) and apparently occupy planes (100) and (010) (Fig. 5B, "LAB-1" and "LAB-2" accordingly). Such geometry of low-angle boundaries, together with the directions of misorientation axes determined for this grain ([001] and [100]), implies several possibilities for present slip systems in this grain:

a. If the rotation axis for low-angle boundary 1 is [001], then it is a tilt boundary with the slip system [100](010).

b. If the rotation axis for low-angle boundary 1 is [100], it is a twist boundary.

c. If the rotation axis for low-angle boundary 1 is [010], it is a tilt boundary with the slip system [100](001).

d. If the rotation axis for the low-angle boundary 2 is [001], it is a tilt boundary with the slip system [010](100).

e. If the rotation axis for the low-angle boundary 2 is [010], it is a twist boundary.

f. If the rotation axis for the low-angle boundary 2 is [100], it is a tilt boundary with the slip system [010](001).

Low-angle boundary traces in grain 15 form stepped rather than straight lines, slightly changing directions over short distances. This low-angle boundary network most likely represents a system of interconnected tilt walls with the slip geometries <100>{010} and <100>{001} and twist walls and may include all possible slip systems a-f, valid for different intervals of a given boundary. Asterism of crystallographic axes is also evidence that there are several slip systems operating at the same time in different grain domains (Moser et al., 2009), indicating spatial heterogeneity of misorientation axes.

In grain 24 (Fig. 5C), one of the low-angle boundaries (“LAB-1”) is straight and parallel to the (100) crystallographic plane. This geometry for low-angle boundary, together with the misorientation axis parallel to [001], implies the slip system [100]{010} for this boundary, because for the tilt boundary slip direction in normal to it and lies in the normal slip plane, whereas rotation axis is parallel to the boundary and normal to the slip direction. The other low-angle boundary in the lower part of the grain extending from left to right (“LAB-2”), has a complicated geometry and most likely represents a result of combination of several slip systems. Minor clusters of misorientation axes around high index directions (Fig. 5C) are either a result of analytical error due to small misorientation angles (e.g. Prior, 1999; Reddy and Buchan, 2005) in this grain, reaching only 3° (see Kovaleva et al., 2016), or evidence of minor slips activated to accommodate strain, connecting major tilt and twist walls that have dispersion around [001]. The second suggestion is also supported by a minor asterism of crystallographic axes in the pole figure (Fig. 5C), which is the evidence of multiple slip systems operating in different small grain domains.

In grain 04, trace of low-angle boundary 1 (“LAB-1”, Fig. 6A) is parallel to the (100) plane (Fig. 6B). Misorientation axes in this grain coincide with the dispersion axis and are parallel to [001] (Fig. 6D). Such geometry implies a tilt boundary correlated with the [100]{010} slip system (Fig. 6B, black lines). Low-angle boundary 2 (“LAB-2”, Fig. 6A) is apparently parallel to the (110) plane, which implies a tilt boundary with the slip system <$\bar{1}$10>{110} and rotation axis [001] (Fig. 6B, grey lines).

In the lower left portion of the crystal 03, the WBV values are small (Fig. 6A, grey solid rectangles), indicating low dislocation density and, therefore, a strain-free domain. In the lower right portion, WBV is dominated by the *a* component (dotted rectangles), which, taking into account rotation axis [001], implies domination of dislocations with the slip system <100>{010}. WBV analyses across the low-angle boundary 1 (“LAB-1”) are dominated by the *b* component (dashed rectangles) that, taking into account rotation axis [001], points to the domination of dislocations with slip along the [010] direction (i.e. slip system <010>{100}, geometrically equivalent to slip system <100>{010}). The WBV analyses across low-angle boundary 2 (“LAB-2”) show high values of the *a* and *b* components, implying the above mentioned slip system <$\bar{1}$10>{110} with slip along the [$\bar{1}$10] plane (Fig. 6B), if the rotation axis geometry is [001]. A highly non-homogeneous distribution of WBV values in grain 03 (Fig. 6A) points to inhomogeneous distribution of post-growth strain, and indicates that the plastic deformation in this zircon is a post-growth process, caused by a directed external differential stress (e.g. MacDonald et al., 2013).

In naturally-deformed crystals, it is difficult to observe pure edge or screw dislocations. Almost all dislocations have both screw and edge components so that they are mixed dislocations (Poirier, 1985). Consistently, summary of our data demonstrate that subgrain walls mostly appear as stepped lines. These walls apparently reflect an interplay between tilt dislocations with the slip systems <100>{010} and <$\bar{1}$10>{110} and rotation axis [001] and twist dislocations with rotation axis [001], and between tilt dislocations with the slip system <100>{001} and twist dislocations with rotation axis [010]. Thus, strain under amphibolite-facies conditions in plastically-deformed zircon grains is accommodated by formation of a continuous network of low-angle boundaries, which formed by a combination of tilt and twist dislocations with above mentioned geometries.

This slip is easily activated when zircon <c> axis has a specific orientation normal or parallel to the vorticity axis of the shear zone (Figs. 7A; 8i and iii). Selective crystal-plastic deformation of zircon grains that are aligned within the XY plane (Fig. 7A) could be explained by the critically resolved shear stress (CRSS) that is more easily reached along specific planes, when the grain orientation is favourable with respect to a local stress field (Hobbs, 1985). Along the <c> axis, the zircon atomic structure consists of chains of alternating edge-sharing SiO_4 tetrahedra and ZrO_8 dodecahedra that are joined laterally by edge-sharing dodecahedra (Robinson et al., 1971; Finch and Hanchar, 2003). To develop a slip in the zircon crystal lattice, it is energetically preferable to break the bonds between SiO_4 tetrahedra and ZrO_8 dodecahedra and displace them along [100], rather than between the strongly bonded ZrO_8 dodecahedra along [001]. Consistently, the geometry of slip systems <100>{010} with the rotation axis [001] are the most frequently observed in zircon (e.g. Leroux, 1999; Reddy et al., 2007; Kovaleva et al., 2014), whereas rotation axis [010] and slip systems <100>{001} are less common (e.g. Kaczmarek et al., 2011). This study agrees with previous investigations (Leroux, 1999; Reddy et al., 2007; Timms et al., 2012; Kovaleva et al., 2014; etc.), and shows that slip along <100>{010} with rotation around [001] is the most energetically preferable geometry. This interpretation is also consistent with the elastic anisotropy of zircon, suggesting rotation around [001] as the least elastic direction, which is most resistant to shearing (Fig. 1). Slip system $<\bar{1}10>\{110\}$, observations of which are reported above, is a newly described (Fig. 6B, “LAB-2”), as such slip system geometry was not reported before.

7. Discussion

7.1. Influence of lattice orientation and elastic anisotropy on deformation behaviour

During simple shear, the vorticity axis is perpendicular to the XZ plane, parallel to the Y axis on the foliation plane and normal to the lineation direction (e.g. schematically shown in Fig. 8, after Reddy and Buchan, 2005). The crystallographic orientations of misorientation axes in plastically-deformed zircon grains, depending on lattice orientation in the simple shear deformation, were observed in Kovaleva et al. (2016) on a large dataset using 6 different samples from a variety of lithologies and shear zones. Our detailed analyses of zircon from one of these samples confirm the earlier results and provides more detailed and accurate data on zircon deformation behaviour. Zircon behaviour in the shear zone is summarized in Fig. 8. Zircon crystals with c-axis oblique to the XY (foliation) plane (>15°) are either undeformed (Fig. 3) or fractured (Figs. 4; 8iv). Grains with <c> oriented at ~15° to the foliation may experience a minor amount of crystal-plastic strain, but, at the same time, can also be fractured (Table 1). Zircon crystals with <c> aligned to the XY plane with <c> parallel or normal to the X direction (stretching lineation) develop misorientation and dispersion axes parallel to [001] (Figs. 7, grains 03, 04, 24, and closely oriented; 8i and iii; Table 1). Grains oriented at 90° usually have additional clusters of misorientation axes. Finally, zircon crystals with <c> aligned in the XY plane at 45° to the X direction reveal two or three misorientation axes, usually orthogonal to each other (e.g. [100] and [001]) in order to accommodate the applied strain (Figs. 5B; 8ii). Misorientation axes in plastically-deformed zircon grains are parallel to the XY plane of a shear zone, where the most strained zircon grains have their misorientation axes parallel to the X direction (Fig. 7B). Less frequently, misorientation axes lie in the YZ plane of a shear zone (Fig. 7B). The observed zircon properties are not in agreement with the model of zircon evolution, suggested by Kaczmarek et al. (2011). These authors implied that that in plastically-deformed grains, where the <c> axis is parallel or normal to the vorticity axis, only one slip system is activated. In contrast, we observed that zircon lattice does not accommodate strain by a single slip system. As a three-dimensional object, zircon should accommodate strain by several slip systems, except for some extreme deformation conditions, such as formation of planar low-angle boundaries (i.e. planar deformation bands) during seismic events (e.g. Kovaleva and Klötzli, 2017). Moreover, Kaczmarek et al. (2011) concluded that in all cases, where the zircon <c> axis is not parallel or normal to the vorticity axis, zircon would necessarily plastically deform and reveal activation along multiple (two or more) glide systems. In our sample, crystal-plastic deformation in grains with <c> orientated at a high angle (>15°) to the foliation plane is not observed (Figs. 3; 4; 7A; Table 1). This discrepancy in the results might be caused by different deformation conditions of the sampled zircon. Finally, Kaczmarek et al. (2011) suggested that "The exact selection of glide-system could be dependant of deformation conditions such as pressure, temperature, and strain rate" [sic], and our observations show that the glide systems depend on the orientation of the zircon crystal in the framework of a host shear zone. Pressure, temperature and strain rate affect the lattice distortion pattern of deformed zircon grains (Piazolo et al., 2012; Kovaleva et al., 2014), but not the glide systems.

The observed properties of misorientation axes are important to document in order to understand zircon rheological behaviour and its evolution in the shear zone. Our observation suggest that the orientation and distribution of misorientation axes in deformed zircon is controlled by the host shear zone, and thus can be used to reconstruct the conditions of deformation, such as tectonic framework and directions of the stress field with respect to deformed zircon (Fig. 8). Because we attribute crystal-plastic deformation of zircon to a specific metamorphic/deformation event, we infer the timing and *P-T* conditions of the event even for detrital and inherited grains. Given that different lattice distortion patterns in zircon are typically restricted to specific stress-strain and metamorphic conditions (e.g. Piazolo et al., 2012; Kovaleva et al., 2014), these patterns may represent a snapshot during potentially complex deformation and metamorphic histories for the shear zone development. Our result demonstrate that analysing a micro-scale microstructures in zircon and its orientation data, analyses of large-scale systems and regional deformation events can be provided. It was recently demonstrated that zircon can act as a mineral chronometer (e.g. Moser et al., 2011; MacDonald et al., 2013; Cavosie et al., 2015; Peterman et al., 2016) and even as mineral thermometer (Timms et al., 2017) for large-scale deformation events, provided careful sample selection for analyses. We suggest that zircon can also act as a structural indicator of tectonic conditions that cause zircon deformation. Positions and distribution of misorientation axes and type of lattice distortion in zircon carry important information about the large-scale processes such as formation of host shear zone, conditions of regional metamorphism, and even timing of metamorphism.

7.2. Implications for zircon geochronology and recommendations

Our work is thus important for the zircon microchemistry and geochronology, as it describes crystal-plastic deformation mechanisms, which should be considered making isotopic and geochemical analyses of zircon from the shear zones. A number of authors demonstrated that crystal-plastic deformation can cause zircon isotopic system resetting (e.g. Reddy et al., 2006, 2007, 2009; Moser et al., 2009, 2011; Timms and Reddy, 2009; Flowers et al., 2010; Reddy and Timms, 2010; Timms et al., 2011, 2012; Piazolo et al., 2012, 2016; MacDonald el al., 2013; Bellucci et al., 2016; Peterman et al., 2016; Kovaleva and Klötzli, 2017; Kovaleva et al., 2017). For example, Peterman et al. (2016) and Piazolo et al. (2016) found toroid-shaped clusters of radiogenic Pb that are associated with dislocations and mark the timing of metamorphism/deformation. It was suggested that radiogenic Pb can be trapped and moved/re-equilibrated by dislocation loops due to increased temperatures associated with metamorphism (Petermant et al., 2016).

There were several attempts to date deformation and metamorphic events in the Earth's crust using plastically-deformed zircon. For example, significant (≥650 Ma) rejuvenation of U-Pb isotopic ages together with CL distortion was documented by Flowers et al. (2010) in zircon grains deformed under granulite-facies conditions. Piazolo et al. (2012) demonstrated that under amphibolite to granulite-facies metamorphic conditions, zircon grains with low-angle boundaries show significant U, Th, and Th/U ratio increase. Consistently, authors indicated younger zircon ages and disturbed CL signal in grains with low-angle boundaries. Piazolo et al. (2012) related this Pb-loss to the presence of interconnected low-angle boundary network, which was formed by imperfectly arranged screw and edge dislocations and resulted in increased pipe diffusion and partial resetting of the isotopic system. Because the conditions of deformation in our sample are similar, and the distortion pattern is the same as in Piazolo et al. (2012), i.e. an interconnected network of low-angle boundaries, formed by mixed (tilt and screw) dislocations, we may expect similar rejuvenation of plastically-deformed zircon in our sample. Moreover, MacDonald et al. (2013) have documented plastically-deformed zircon grains with Pb-Pb distorted isotopic ages that correspond, within an error, to the regional amphibolite-facies metamorphic event. In that case, crystal-plastic deformation of zircon occurred, as in our sample, under amphibolite-facies conditions, and lead to a complete resetting of isotopic ages. With the help of our finding one cannot only attempt dating the deformation event, using certain grains in a shear zone, but also attribute different microstructures to distinct stress-strain fields, which were active at different times during the evolution of the geological units. Mineral dating and interpretations can be done *in situ* based on the orientation of the zircon grains and their misorientation axes and glide systems within the host shear zone.

Conclusions

In this work, we demonstrate mechanisms of strain accommodation in zircon under the amphibolite-facies conditions during the simple shear deformation. We demonstrate that the resulting geometry of dislocations and slip systems in zircon are mainly determined by zircon elastic anisotropy and, at the same time, by crystallographic orientation of the zircon in the shear zone. In particular, zircon deforms plastically if it <c> axis lies parallel to the foliation plane, with the majority of deformed grains having their <c> axes aligned with the lineation. To accommodate strain, zircon develops an interconnected network of stepped low-angle boundaries, formed by tilt dislocations with the slip systems <100>{010} and <$\bar{1}$10>{110} and rotation axis [001], twist dislocations with rotation axis [001], and tilt dislocations with the slip system <100>{001} and rotation axis [010]. The slip system $\langle\bar{1}10\rangle\{110\}$ with rotation axis [001] has not been previously reported in zircon. Observed slip planes are conditioned by the shape of zircon Young's modulus, which has high values along the low indices planes and maximum value in zircon basal plane. Poisson ratio and Shear modulus have the maximum values parallel to [001], defining the most energetically favourable and thus the most common rotation axis in zircon crystal lattice. Zircon crystals, hosted by rheologically weak phases, also tend to develop [001] rotation axes.

Misorientation axes of plastically-deformed zircon grains are, in most cases, oriented parallel to the XY plane of the sample and are often parallel to zircon <c> axis. In a few cases misorientation axes are parallel to YZ plane of a sample, where the strain degree is comparatively low.

Our finding is significant for zircon geochronology and can be useful when reconstructing the history and structural elements of polymetamorphic terrains. We demonstrate how micro-scale structures can be relevant for studying large-scale and even regional events.

Acknowledgements

This study was funded by the University of Vienna (doctoral school "DOGMA", project IK 052) and the Austrian Science Foundation Fund (FWF): I471-N19, which is part of the DFG-FWF funded international research group FOR741-DACH. The authors acknowledge access to the Laboratory for scanning electron microscopy and focused ion beam applications, Faculty of Earth Sciences, Geography and Astronomy at the University of Vienna (Austria). Authors are grateful to Claudia Beybel, Franz Biedermann, Bernhard Grasemann, Sigrid Hrabe, Hugh Rice, Markus Palzer, Nicholas Timms, Claudia Trepmann, and all colleagues of the FOR741 research group for fruitful discussions and comments. Thanks goes to Matthew Huber for his support, and for checking the text for spelling and grammar. Insightful comments and suggestions of the editor William Dunne, reviewer Elena Druguet and anonymous reviewers helped to improve this manuscript greatly.

References

Bachmann, F., Hielscher, R., Schaeben, H., 2010, Texture Analysis with MTEX – Free and Open Source Software Toolbox. Solid State Phenomena 160, 63-68.

Bachmann, F., Hielscher, R., Schaeben, H., 2011, Grain detection from 2d and 3d EBSD data-specification of the MTEX algorithm. Ultramicroscopy 111, 1720-1733.

Bass, J. D., 1995. Elasticity of minerals, glasses and melts. In: Ahrens, T.J. (Ed.), Mineral Physics and Crystallography: a Handbook of Physical Constants. American Geophysical Union, Washington DC, 45–63.

Bellucci, J.J, Whitehouse, M.J., Nemchin, A.A., Snape, J.F., Pidgeon, R.T., Grange, M., Reddy, S.M., Timms, N.E., 2016. A scanning ion imaging investigation into the micron-scale U-Pb systematics in a complex lunar zircon. Chemical Geology 438, 112-122.

Bestmann, M., Prior, D.J., 2003. Intragranular dynamic recrystallization in naturally deformed calcite marble: diffusion accommodated grain boundary sliding as a result of subgrain rotation recrystallization. Journal of Structural Geology 25, 1597–1613.

Cavosie, A.J., Erickson, T.M., Timms, N.E., Reddy, S.M., Talavera, C., Montalvo, S.D., Pincus, M.R., Gibbon, R.G., Moser, D., 2015. A terrestrial perspective on using ex situ shocked zircons to date lunar impacts. Geology 43, 999–1002.

Davis, D.W., Williams, I.S., Krogh, T.E., 2003. Historical development of zircon geochronology. In: Hanchar, J.M., Hoskin, P.W.O. (Eds.), Zircon. Mineralogical Society of America and Geochemical Society, Reviews in Mineralogy and Geochemistry, 53, Washington D.C., 145–181.

Den Toonder, J.M.J, van Dommelen, J.A.W., Baaijens, F.P.T., 1999. The relation between single crystal elasticity and the effective elastic behaviour of polycrystalline materials: theory, measurement and computation. Modelling and Simulation in Materials Science and Engineering 9, 909–928.

Drury, M.R., Urai, J.L., 1990. Deformation-related recrystallization processes. Tectonophysics 172, 235-253.

Finch, R.J., Hanchar, J.M., 2003. Structure and Chemistry of Zircon and Zircon-Group Minerals. In: Hanchar, J. M., Hoskin, P. W. O., eds. Zircon. Mineralogical Society of America and Geochemical Society, Reviews in Mineralogy and Geochemistry 53, 1-26.

Flowers, R.M., Schmitt, A.K., Grove, M., 2010. Decoupling of U–Pb dates from chemical and crystallographic domains in granulite facies zircon. Chemical Geology 270, 20–30.

Hansen, L.N., Warren, J.M., 2015. Quantifying the effect of pyroxene on deformation of peridotite in a natural shear zone. , Journal of Geophysical Research: Solid Earth 120, 2717–2738.

Hobbs, B.E., 1985. The geological significance of microfabric analysis. In: Wenk, H.R. (Ed.), Preferred orientation in deformed metal and rocks. An introduction to modern texture analysis, Academic Press, Inc., Orlando, Florida, 463–484.

Hobbs, B.E., 1968. Recrystallization of single crystals of quartz. Tectonophysics 6, 353-401.

Kaczmarek, M.A., Reddy, S.M., Timms, N.E., 2011. Evolution of zircon deformation mechanisms in a shear zone (Lanzo massif, Western-Alps). Lithos 127, 414-426.

Kenkmann, T., 2000. Processes controlling the shrinkage of porphyroclasts in gabbroic shear zones. Journal of Structural Geology 22, 471-487.

Kovaleva, E., Klötzli, U., 2017. NanoSIMS study of seismically deformed zircon: Evidence of Y, Yb, Ce and P re-distribution and resetting of radiogenic Pb. American Mineralogist, in press.

Kovaleva, E., Klötzli, U., Habler, G., Libowitzky, E., 2014. Finite lattice distortion patterns in plastically deformed zircon grains. Solid Earth 6, 1799-1861.

Kovaleva, E., Klötzli, U., Habler, G., 2016. On the geometric relationship between deformation microstructures in zircon and the kinematic framework of the shear zone. Lithos 262, 192-212.

Kovaleva, E., Klötzli, U., Habler, G., Huet, B., Guan, Y., Rhede, D., 2017. The effect of crystal-plastic deformation on isotope and trace element distribution in zircon: Combined BSE, CL, EBSD, FEG-EMPA and NanoSIMS study. Chemical Geology 450, 183-198.

Kruse, R., Stuenitz, H., Kunze, K., 2001. Dynamic recrystallization processes in plagioclase porphyroclasts. Journal of Structural Geology, 23, 1781–1802.

Leroux, H., Reimold, W.U., Koeberl, C., Hornemann, U., Doukhan, J.C., 1999. Experimental shock deformation in zircon: a transmission electron microscopic study. Earth and Planetary Science Letters 169, 291–301.

MacDonald, J.M., Wheeler, J., Harley, S.L., Mariani, E., Goodenough, K.M., Crowley, Q., Tatham, D., 2013. Lattice distortion in a zircon population and its effects on trace element mobility and U–Th–Pb isotope systematics: examples from the Lewisian Gneiss Complex, northwest Scotland. Contributions to Mineralogy and Petrology 166, 21–41.

Mainprice, D., Hielscher, R., Schaeben, H., 2011, Calculating anisotropic physical properties from texture data using the MTEX open source package. In: Prior, D.J., Rutter, E.H., Tatham, D.J. (Eds.), Deformation Mechanisms, Rheology and Tectonics: Microstructures, Mechanics and Anisotropy. Geological Society, London, Special Publications 360, 175-192.

Menegon, L., Nasipuri, P., Stünitz, H., Behrens, H., Ravna, E., 2011. Dry and strong quartz during deformation of the lower crust in the presence of melt. Solid Earth 116, B10, doi:10.1029/2011JB008371

Miller, C., Konzett, J., Tiepolo, M., Armstrong, R.A., Thöni, M., 2007. Jadeite-gneiss from the eclogite zone, Tauern Window, Eastern Alps, Austria: metamorphic, geochemical and zircon record of a sedimentary protholith. Lithos 93, 68-88.

Moser, D.E., Davis, W.J., Reddy, S.M., Flemming, R.L., Hart, R.J., 2009. Zircon U–Pb strain chronometry reveals deep impact-triggered flow. Earth and Planetary Science Letters 277, 73–79.

Moser, D. E., Cupelli, C.L., Barker, I.R., Flowers, R.M., Bowman, J.R., Wooden, J., Hart, J.R., 2011. New zircon shock phenomena and their use for dating and reconstruction of large impact structures revealed by electron nanobeam (EBSD, CL, EDS) and isotopic U–Pb and (U–Th)/He analysis of the Vredefort dome. Canadian Journal of Earth Sciences 48, 117–139.

Özkan, H., Jamieson, J.C., 1978. Pressure dependence of the elastic constants of nonmetamict zircon. Physics and Chemistry of Minerals 2, 215-224.

Pennacchioni, G., Mancktelow, N.S., 2007. Nucleation and initial growth of a shear zone network within compositionally and structurally heterogeneous granitoids under amphibolite facies conditions. Journal of Structural Geology 29, 1757-1780.

Peterman, E.M., Reddy, S.M., Saxey, D.W., Snoeyenbos, D.R., Rickard, W.D.A., Fougerouse, D., Kylander-Clark, R.A.C., 2016. Nanogeochronology of discordant zircon measured by atom probe microscopy of Pb-enriched dislocation loops. Science Advances 2, e1601318.

Piazolo, S., Austrheim, H., Whitehouse, M., 2012. Brittle-ductile microfabrics in naturally deformed zircon: Deformation mechanisms and consequences for U-Pb dating. American Mineralogist 97, 1544–156.

Piazolo, S., La Fontaine, A., Trimby, P., Harley, S., Yang, L., Armstrong, R., Cairney, J.M., 2016. Deformation-induced trace element redistribution in zircon revealed using atom probe tomography. Nature Communications 7, 10490.

Poirier, J. P., 1985. Creep of Crystals: High-Temperature Deformation Processes in Metals, Ceramics and Minerals. Cambridge University Press, New York.

Poirier, J.P., Nicolas, A., 1975. Deformation-induced recrystallization by progressive misorientation of subgrain-boundaries, with special reference to mantle peridotites. Journal of Geology 83, 707-720.

Prior, D.J., 1999. Problems in determining the orientation of crystal misorientation axes for small angular misorientations, using electron backscatter diffraction in the SEM, Journal of Microscopy 195, 217-225.

Prior, D.J., Rutter, E.H., Tatham, D.J., 2011. Deformation mechanisms, rheology and tectonics: microstructures, mechanics and anisotropy: introduction. In: Prior, D.J., Rutter, E.H., Tatham, D.J. (Eds.), Deformation mechanisms, rheology and tectonics: Microstructures, mechanics and anisotropy. Geological Society Special Publications 360, London, 1-5.

Reddy, S.M., Buchan, C., 2005. Constraining kinematic rotation axes in high-strain zones: a potential microstructural method? In: Gapais, D., Brun, J.P., Cobbold, P.R. (Eds.), Deformation mechanisms, rheology and tectonics: from mineral to the lithosphere, 243. Special Publications, Geological Society, London, 1–10.

Reddy, S.M., Timms, N.E., 2010. Deformation of zircon and implications for geochemistry and geochronology. Source Abstracts with Programs - Geological Society of America 42, 634.

Reddy, S.M., Timms, N.E., Trimby, P., Kinny, P.D., Buchan C., Blake K., 2006. Crystal-plastic deformation of zircon: a defect in the assumption of chemical robustness. Geology 34, 257-260.

Reddy, S.M., Timms, N.E., Pantleon, W., Trimby, P., 2007. Quantitative characterization of plastic deformation of zircon and geological implications. Contributions to Mineralogy and Petrology 153, 625–645.

Reddy, S.M., Timms, N.E., Hamilton, P.J., Smyth, H.R., 2009. Deformation-related microstructures in magmatic zircon and implications for diffusion. Contributions to Mineralogy and Petrology 157, 231–244.

Robinson, K., Gibbs, G. V., Ribbe, P. H., 1971. The structure of zircon: a comparison with garnet. American Mineralogist 56, 782-790.

Schmid, D.W., Podladchikov, Y.Yu., 2005. Mantled porphyroclast gauges. Journal of Structural Geology 27, 571–585.

Selverstone, J., Morteani, G., Staude, J.-M., 1991. Fluid channelling during ductile shearing: transformation of granodiorite into aluminous schist in the Tauern Window, Eastern Alps. Journal of Metamorphic Geology 9, 419–431.

Timms, N.E., Reddy, S.M., 2009. Response of cathodoluminescence to crystal-plastic deformation in zircon. Chemical Geology 261, 11–23.

Timms, N.E., Kinny, P., Reddy, S.M., Evans K., Clark C., Healy D., 2011. Relationship among titanium, rare earth elements, U–Pb ages and deformation microstructures in zircon: Implications for Ti-in-zircon thermometry. Chemical Geology 280, 33–46.

Timms, N.E., Reddy, S.M., Healy, D., Nemchin, A.A., Grange, M.L., Pidgeon, R.T., Hart, R., 2012. Resolution of impact-related microstructures in lunar zircon: a shock-deformation mechanism map. Meteoritics & Planetary Science 47, 120–141.

Timms, N.E., Erickson, T.M., Zanetti, M.R., Pearce, M.A., Cayron, C., Cavosie, A.J., Reddy, S.M., Wittmann, A., Carpenter, P.K., 2017. Cubic zirconia in >2370° C impact melt records Earth's hottest crust. Earth and Planetary Science Letters 477, 52–58.

Veselá, P., Söllner, F., Finger, F., Gerdes, A., 2011. Magmato-sedimentary Carboniferous to Jurassic evolution of the western Tauern window, Eastern Alps (constraints from U-Pb zircon dating and geochemistry). International Journal of Earth Sciences 100, 993–1027.

Wheeler, J., Mariani, E., Piazolo, S., Prior, D. J., Trimby, P., Drury, M. R., 2009. The Weighted Burgers Vector: a new quantity for constraining dislocation densities and types using Electron Backscatter Diffraction on 2D sections through crystalline materials. Journal of Microscopy 233, 482-494.

Wheeler, J., Mariani, E., Piazolo, S., Prior, D. J., Trimby, P., Drury, M. R., 2012. The Weighted Burgers Vector: a quantity for constraining dislocation densities and types using Electron Backscatter Diffraction on 2D sections through crystalline materials. Materials Science Forum 715-716, 732-736.

White, S., 1973. Syntectonic recrystallization and texture development in quartz. Nature 244, 276-278.

Figure captions

Figure 1. Visualization of zircon elastic properties as a function of crystallographic geometry. A. Young's modulus. B. P waves velocity. C. Poisson ratio. D. Shear modulus. Elastic constants after Özkan and Jamieson (1978), Bass et al. (1995) and den Toonder et al. (1999). Solid black circles with labels indicate main crystallographic directions in zircon.

Figure 2. A. and B. Optical microscope images (cross-polarized light) of the thin sections. Foliation and compositional layering are outlined (dotted white line) and labelled. Numbers indicate positions of studied crystal-plastically deformed zircon grains (for more positions refer to Supplemental Fig. 1). C. and D. Petrographic context of zircon grains within the analysed sample (BSE images). Bt = biotite, Chl = chlorite, Kfs = K-feldspar, Pl = plagioclase, Qtz = quartz, Ttn = titanite, Zrn = zircon.

Figure 3. Microstructural data of unstrained zircon from the sampled meta-lamprophyre. Cumulative EBSD maps (left column), user-selected reference point marked with a white star. EBSD pattern quality maps (middle column), patchy inhomogeneities in C indicate surface contamination of the sample by polishing material. Lower hemisphere equal-area projections (right column) show the position of <c> of the corresponding grain (empty circles). The foliation plane in the figures is subhorizontal. Dotted grey circles indicate the direction of stretching lineation.

Figure 4. Microstructural data for fractured zircon. Orientation contrast images of grains with brittle deformation (left column). Zrn = zircon. Lower hemisphere equal-area projections (right column) with inferred position of long axes of corresponding grains (empty circles). The foliation plane in the figures is subhorizontal. Dotted grey circles indicate the direction of stretching lineation.

Figure 5. Crystal-plastically deformed zircon crystals: microstructural data, modified from Kovaleva et al. (2016). Left column: EBSD pattern quality images. Arrows point to low-angle boundary network (dark-grey stepped lines). Light-grey areas, separated by low-angle boundaries are subgrains. Middle column: pole figures with lower hemisphere projections of zircon crystallographic directions. Labels in square braces ([]) indicate main crystallographic axes, black lines are reconstruction of the subgrain boundary planes. The foliation plane in the figures is subhorizontal. The direction of the lineation is highlighted by dotted grey circles. Arrows in (A) indicate the rotation of all crystallographic directions about [001], which is the least dispersed. Right column: inversed pole figures with misorientation axes density contours with scale bars, numbers are crystallographic directions of zircon.

Figure 6. A. Local misorientation map of deformed grain 04. Weighted Burgers Vector (WBV) components are indicated by rectangular subareas. Grey rectangles show the areas with WBV that are comparatively small, indicating no strain. Dotted and dashed rectangles show areas with WBV dominated by the *a* or *b* components, respectively. Black rectangles show areas with WBV with mixed components. B. Reconstruction of the low-angle boundaries and slip systems of grain 04 plotted in the pole figure with lower hemisphere projections of zircon crystallographic directions. Thick lines outside the circle indicate the direction of the low-angle boundary traces. Solid lines inside the circle indicate the reconstruction of low-angle boundary planes. Dashed lines indicate the reconstruction of slip planes for the low-angle boundaries highlighted in A. Elements that correspond to low-angle boundary 1 ("LAB-1") are indicated in black. Elements that correspond to low-angle boundary 2 ("LAB-2") are indicated in grey. The small circle highlights the dispersion and misorientation axis. C. EBSD pattern quality image of grain 04. Horizontal dark line in the upper part is a scratch. D. Inversed pole figure with a scale bar, showing misorientation axes density contours, numbers are crystallographic directions of zircon.

Figure 7. A. Pole figure with <c> positions of analysed zircon grains, adopted from Kovaleva et al. 2016. Labels in angle brackets (<>) indicate misorientation axes for the corresponding grains. The grey dashed line shows the direction of the foliation. The grey dotted circle shows the direction of lineation. Solid black circles correspond to <c> directions of grains that are plastically-deformed. Empty circles correspond to unstrained or fractured zircon grains, grey circle shows the orientation of a grain with very minor degree of strain. B. Pole figure with directions of the misorientation axes (indicated by circles) within the sampled shear zone. Misorientation axes of deformed grains analysed in this study are labelled with the

corresponding numbers. Circles are color-coded according to the total amount of strain corresponding to the cumulative misorientation angle and the number of low-angle boundaries, using a 0 to 10 scale, where 10 (black circles) are the most strained grains and 0 (white) are the least strained in the population.

Figure 8. Schematic sketch showing how zircon deformation evolution depends on its orientation in the macroscopic kinematic frame. Cases (i), (ii) and (iii) indicate plastic deformation, (iv) indicates unstrained and fractured grains with c-axes at a high angle to the foliation. (i) <c> is parallel to the vorticity axis, the misorientation axis is parallel to [001]. (ii) Grain with <c> at an angle 45° to the kinematic rotation axis develops [001] and [100] rotation axes. (iii) <c> is normal to the kinematic rotation axis, and the rotation axis is parallel to [001]. Misorientation axes in cases i-iii are parallel to the XY plane of the shear zone.

	Grain #	Types of analyses	Host phase(s)	Type of deformation	Degree of crystal-plastic strain (0-10)	Orientation of <c> axis in the shear zone	Orientation of misorientation axes	Orientation of misorientation axes in the shear zone
Thin section A	01 (Fig. 3A)	EBSD maps	Biotite	None	0	High angle to the foliation	N/A	N/A
	03 (Fig. 5A)		Chlorite and K-feldspar interface	Cr-pl. type III, stepped LABs	10	Parallel to lineation	[001]	Parallel to lineation
	03b		Biotite	Cr-pl. type III, one semi-circular LAB	2		<212>	Subparallel to foliation at 55° to lineation
	04 (Fig. 6)		Biotite with titanite pressure shadow	Cr-pl. type III, stepped LABs	4	Subparallel to lineation	[001], minor <212>	Parallel to lineation; ~15° to foliation at 45° to lineation
	09		Quartz, plagioclase and biotite interface	Brittle and minor cr-pl. type II (semi-circular bending at the grain margin), stepped fracture	3	About 15° to foliation and 55° to lineation	[001], *<311>*	Same as <c> axis
	10 (Fig. 3B)		Plagioclase and quartz interface	None	0	>20° to foliation and 50° to lineation	N/A	N/A
	16 (Fig. 3C)		Plagioclase	None	0	More than 50° from foliation and lineation		
	20		Biotite with titanite pressure shadow	Cr-pl. type III, stepped LAB	1	Parallel to foliation and at 45° to lineation	<101>, <310>, *minor <511>*	Parallel to foliation at 90° to lineation; normal to foliation and to lineation
Thin section B	15 (Fig. 5B)	OCI and EBSD map	Biotite	Cr-pl. type III, stepped LABs	5		[001], <100>	Parallel to foliation at 45° to lineation; 15° to foliation at 50° to lineation
	15b	OCI		None	0	Unknown	N/A	N/A
	16							
	19a		Biotite, K-feldspar and epidote					
	19b					Long axis is at a high angle to foliation		

	19c		K-feldspar			Unknown		
	20	OCI and EBSD map	Plagioclase	Brittle and cr-pl. type III, stepped LABs and curved fracture	4	15° to foliation 45° to lineation	<201>, <321>	Subparallel to YZ plane at 55° to foliation; subparallel to foliation at 30° to lineation
	23	OCI	Plagioclase and K-feldspar	Cr-pl. type III, stepped LABs	1	Unknown	N/A	N/A
	24 (Fig. 5C)	OCI and EBSD map	Biotite and plagioclase	Cr-pl. type III, stepped and curved LABs	3	Subparallel to foliation at 90° to lineation	[001], *minor <212>, <321>, <110>*	Same as <c> axis
	24a	OCI	Plagioclase and K-feldspar	None	0	Unknown	N/A	N/A
	24c							
	24d	OCI and EBSD maps	Biotite and plagioclase	Very minor cr-pl. type III, jigsaw-shaped LABs	0.5	High angle to foliation and to lineation	[001], *<112>, <312>*	Subparallel to YZ plane ~70° to foliation at 85° to lineation
	25		K-feldspar, titanite, rutile	Cr-pl. type III, one rounded LAB	2	Subparallel to foliation and at 10° to lineation	<210>	15° to foliation at 55° to lineation
	26		Biotite	Cr-pl. type III, stepped LABs	9	5° to foliation and 10° to lineation	[001]	Same as <c> axis
	27	OCI	Chlorite and K-feldspar	None	0	Unknown	N/A	N/A
	28	OCI and EBSD map	Biotite	Cr-pl. type III, stepped LABs	6	Parallel to lineation	[001]	Parallel to lineation
	31a (Fig. 4B)	OCI	Biotite and K-feldspar	Brittle, stepped fracture	0	Long axis is at high angle to foliation	N/A	N/A
	31b	OCI and EBSD map	Biotite	Cr-pl. type III, stepped LABs	6	Parallel to lineation	[001], *minor <212>, <311>*	Parallel to lineation
	32a	OCI	K-feldspar, titanite and plagioclase	Cr-pl. type III (very minor), stepped LAB	0.5	Unknown	N/A	N/A
	32b			Brittle, curved fracture	0			
	33 (Fig. 4A)		Plagioclase and biotite	Brittle, subparallel fractures		Long axis is at high angle to foliation		
	36		Biotite	None		Unknown		
	37a							

Table 1. Orientation and microstructural data for the zircon grains, analysed in this study. OCI = orientation contrast imaging, Cr-pl. = crystal-plastic, LAB = low-angle boundary. In italic – minor misorientation axes directions that are not plotted in Fig. 7B. Degree of strain is empirically evaluated, based on (1) amount and density of low-angle boundaries, and, where applicable, (2) cumulative misorientation within the grain.

Figure 1

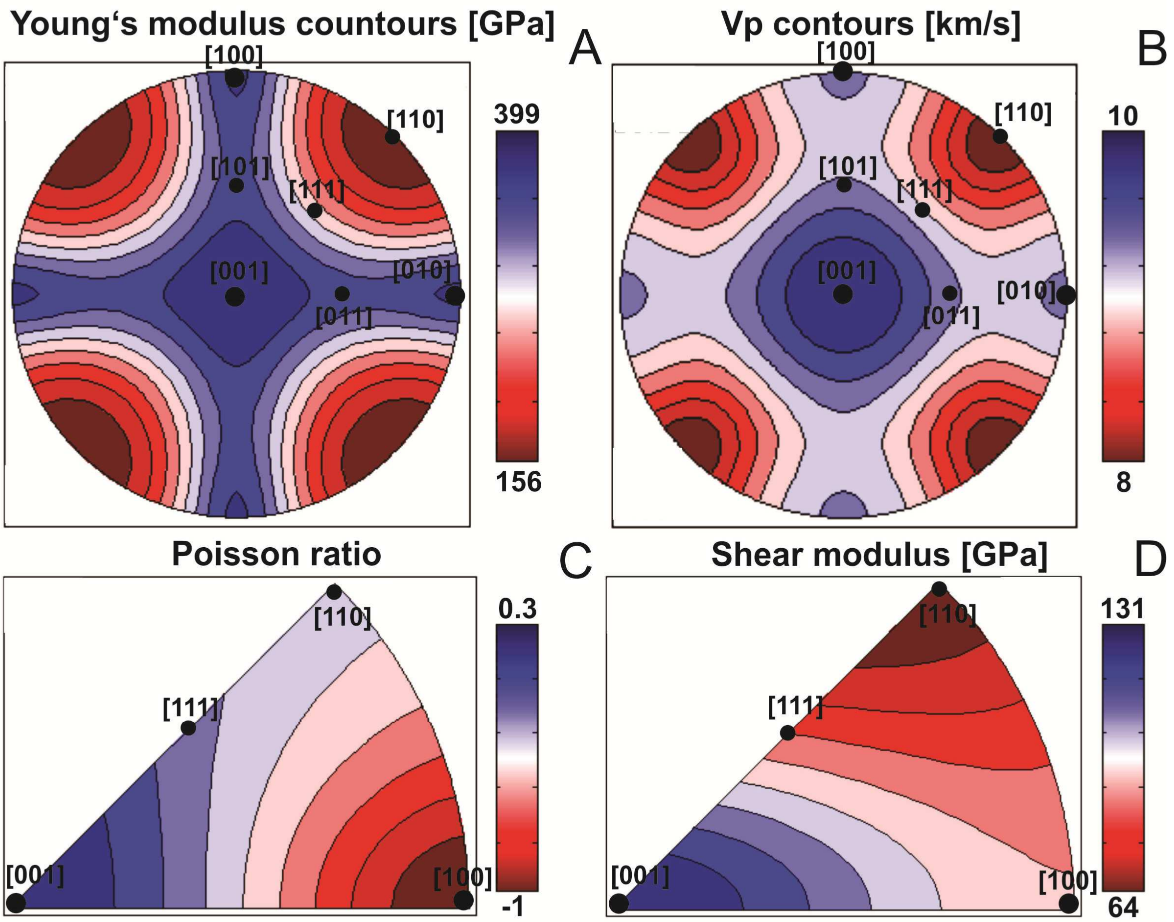
Young's modulus countours [GPa]
A
[100]
[110]
[101]
[111]
[001]
[011]
[010]
399
156
Vp contours [km/s]
B
[100]
[110]
[101]
[111]
[001]
[011]
[010]
10
8
Poisson ratio
C
[110]
[111]
[001]
[100]
0.3
-1
Shear modulus [GPa]
D
[110]
[111]
[001]
[100]
131
64

Figure 2

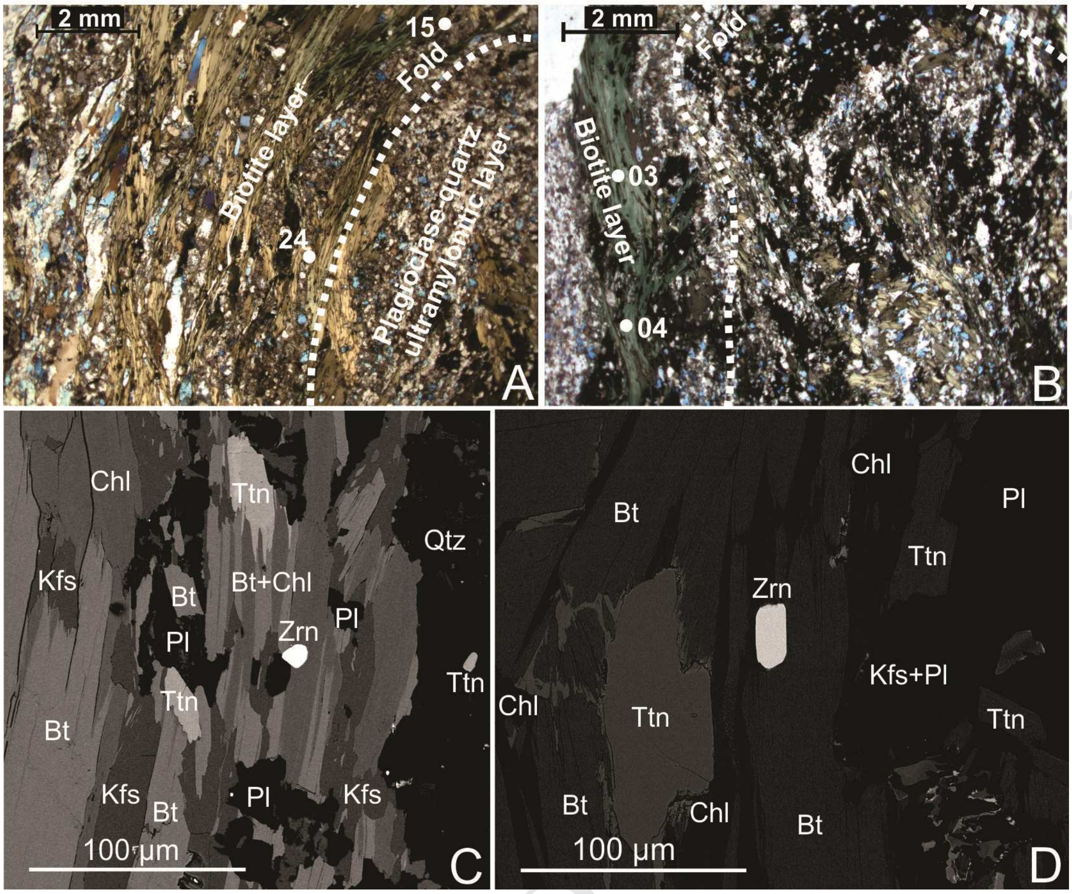
2 mm
15
Fold
Biotite layer
24
Plagioclase-quartz ultramylonitic layer
A
2 mm
Fold
Biotite layer
03
04
B
Chl
Ttn
Qtz
Kfs
Bt
Bt+Chl
Pl
Zrn
Pl
Ttn
Ttn
Bt
Kfs
Bt
Pl
Kfs
100 µm
C
Chl
Bt
Pl
Ttn
Zrn
Kfs+Pl
Chl
Ttn
Ttn
Bt
Chl
Bt
100 µm
D

Figure 3

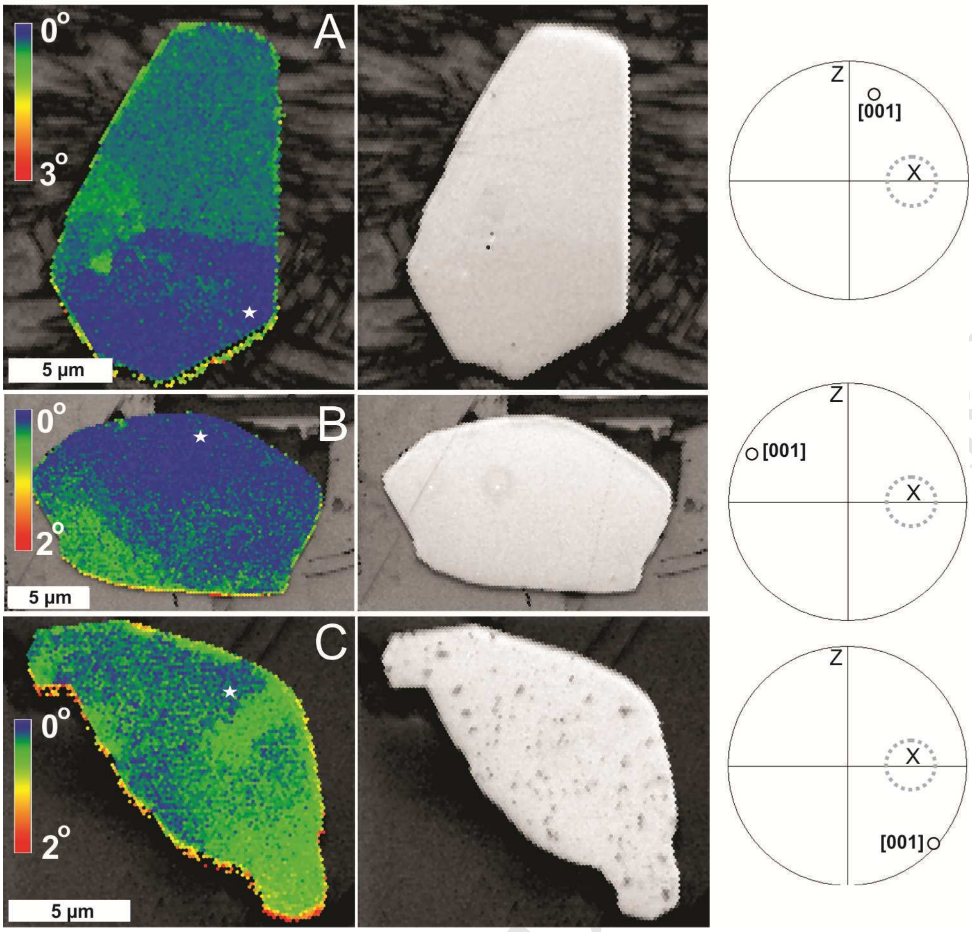

Figure 4

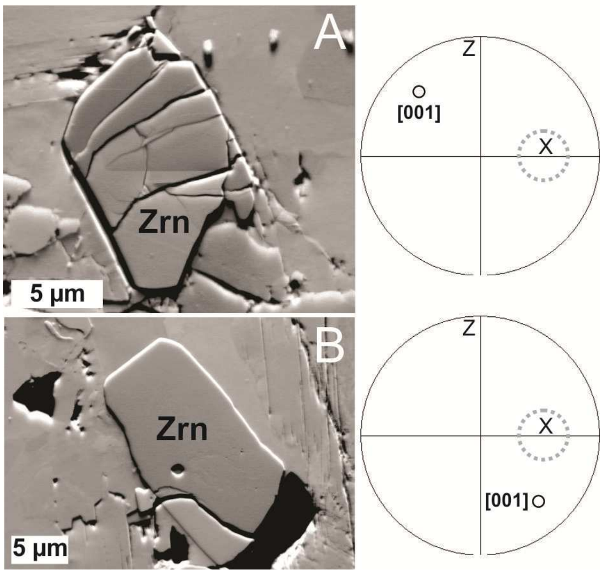

Figure 5

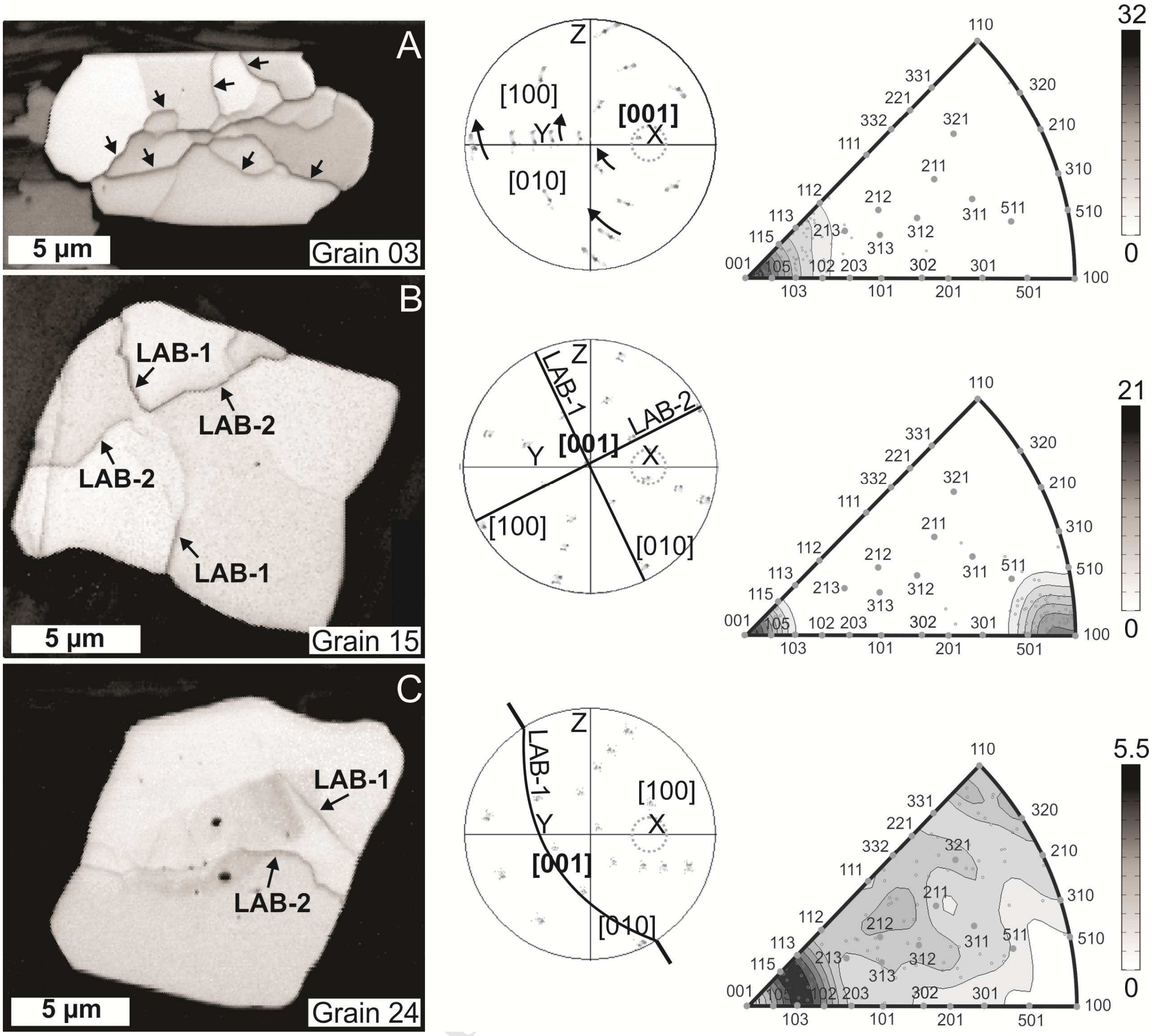

A
5 µm
Grain 03
Z
[100]
Y
[001]
X
[010]
B
LAB-1
LAB-2
LAB-2
LAB-1
5 µm
Grain 15
C
LAB-1
LAB-2
5 µm
Grain 24
32
21
5.5
0
110
331
320
221
321
332
210
111
211
310
112
212
311
511
510
113
213
312
115
313
001
105
102
203
302
301
100
103
101
201
501

Figure 6

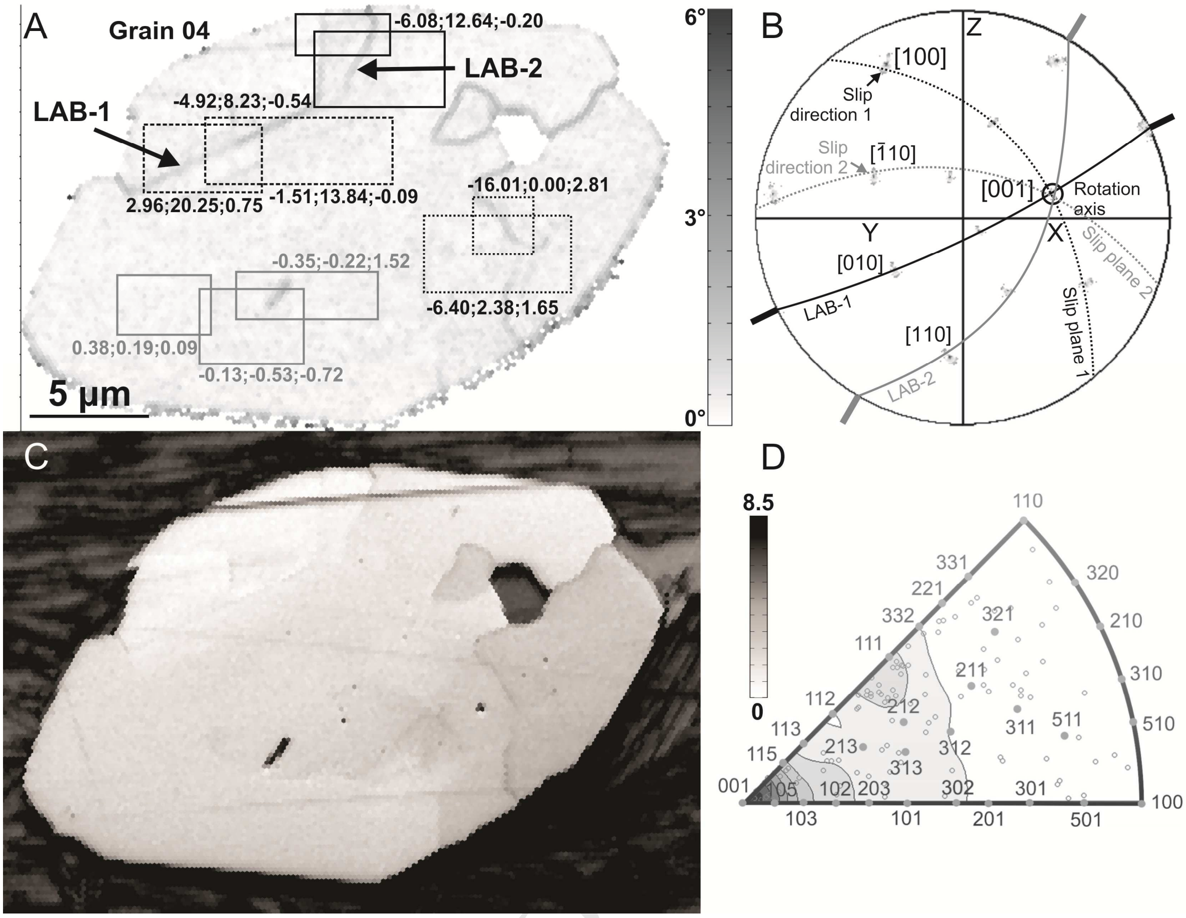
A
Grain 04
LAB-1
LAB-2
-6.08;12.64;-0.20
-4.92;8.23;-0.54
2.96;20.25;0.75
-1.51;13.84;-0.09
-16.01;0.00;2.81
-6.40;2.38;1.65
-0.35;-0.22;1.52
0.38;0.19;0.09
-0.13;-0.53;-0.72
5 µm
6°
3°
0°
B
Z
Y
X
[100]
Slip direction 1
Slip direction 2
[1̄10]
[001]
Rotation axis
[010]
[110]
Slip plane 1
Slip plane 2
LAB-1
LAB-2
C
D
8.5
0
110
331
320
221
321
332
210
111
211
310
112
212
511
510
113
311
312
115
213
313
001
105
102
203
302
301
100
103
101
201
501

Figure 8

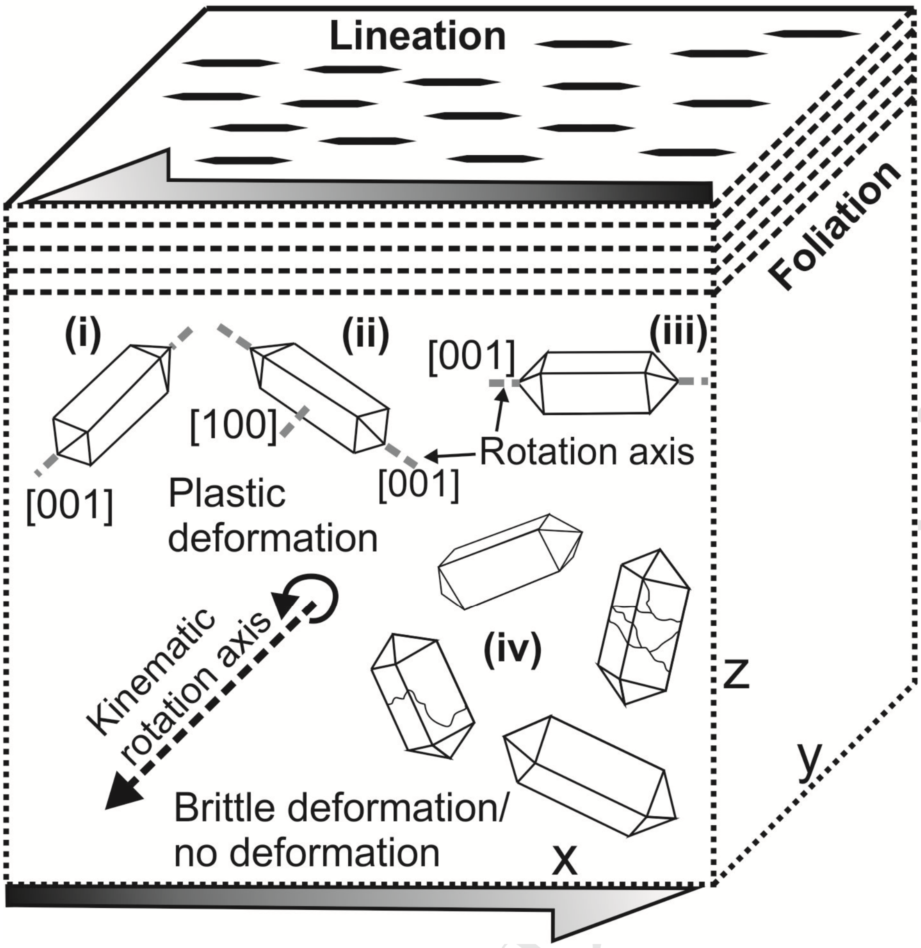

Lineation
Foliation
(i)
(ii)
(iii)
[001]
[100]
[001]
[001]
Rotation axis
Plastic
deformation
Kinematic
rotation axis
(iv)
z
y
Brittle deformation/
no deformation
x

Figure 7

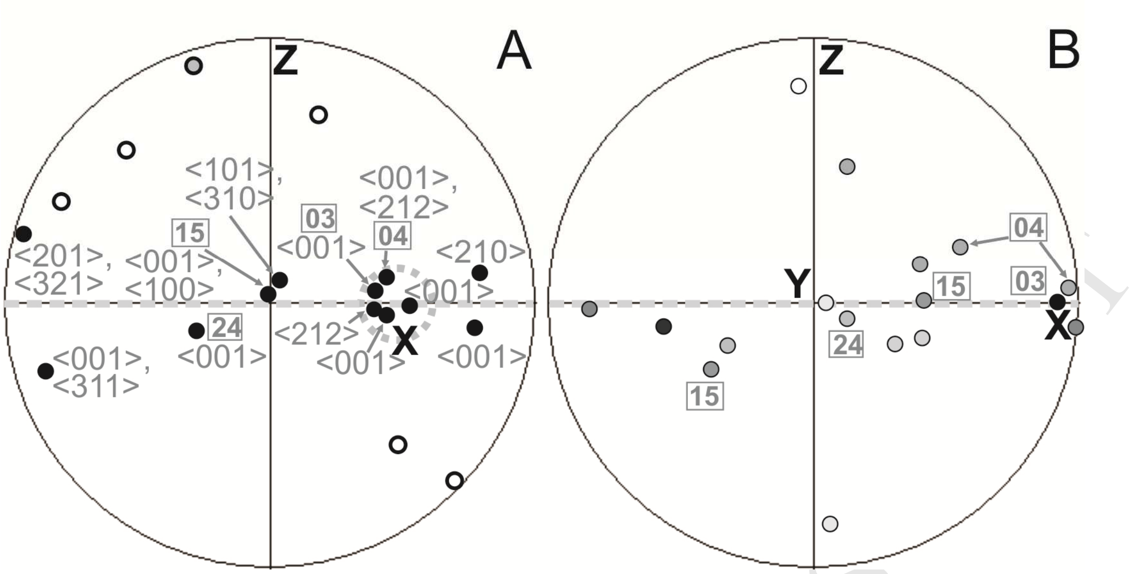

A
B
Z
X
Y
<101>,
<310>
<001>,
<212>
03
04
15
24
<001>
<210>
<201>,
<321>
<001>,
<100>
<212>
<001>,
<311>

- Under amphibolite-facies zircon forms a network of low-angle boundaries by switching between tilt and twist dislocations with [010] and [001] rotation axes
- Documented tilt dislocations have <100>{010}, <100>{001} and <-110>{110} geometry
- Elastic anisotropy properties of zircon influence its rheological behavior
- The rotation axis [001] is conditioned by high Young's modulus values along this direction
- The slip system <-110>{110} is newly described for zircon